Geochemistry, Geophysics, Geosystems

Supporting Information for

The dynamics of unlikely slip: 3D modeling of low-angle normal fault rupture at the Mai'iu fault, Papua New Guinea

James Biemiller[1], Alice-Agnes Gabriel[1,2], Thomas Ulrich[2]

[1]Institute of Geophysics and Planetary Physics, Scripps Institution of Oceanography, University of California San Diego, La Jolla, California, USA.

[2]Department of Earth and Environmental Sciences, Ludwig Maximillian University of Munich, Munich, Germany.

Contents of this file

Introduction

The supporting text details the rate-and-state friction equations solved in the dynamic rupture simulations (text S1) and the procedure for ensuring sufficiently fine mesh resolution in these models (text S2). The supporting figures detail results from additional dynamic rupture simulations probing model sensitivity and performed alongside the four primary models described in the main text, including models with alternate pre-stresses that are initially farther from failure (figure S1), models with alternate pore fluid pressures (figure S2), variants of Model 3 with stronger imposed nucleation conditions (figure S3), models with planar detachment fault geometries (figure S4), and models without velocity-strengthening materials in the shallow parts of the fault (figure S5). The supporting table S1 details the parameters varied between the different models presented in the supporting figures.

Text S1. Rate-and-state friction with fast velocity-weakening

Following recent models that have unraveled complex and/or poorly instrumented events in various tectonic contexts (Ulrich et al., 2019a, 2019b; Palgunadi et al., 2020) we use a rate-and-state friction law with enhanced velocity-weakening (e.g., Dunham et al., 2011a) that accounts for the rapid frictional weakening at coseismic slip rates observed in high-velocity laboratory friction experiments (e.g., DiToro et al., 2011). This friction law has been benchmarked by the Southern California Earthquake Center in community benchmark problem TPV104 (Harris et al., 2018).

Fault strength governs the magnitude of shear traction τ as determined by the product of the effective normal stress σ_n' and the instantaneous friction coefficient *f,*

$$\tau = f(V, \psi)\sigma_n', \quad \text{(S1)}$$

where ψ is the state variable. Parallel traction (τ) and slip rate (V) vectors satisfy:

$$\tau V = V\tau. \quad \text{(S2)}$$

Instantaneous friction is computed from the current values of the state variable ψ and slip rate V and depends on the direct-effect parameter a and the reference velocity V_0

$$f(V, \psi) = asinh^{-1}\left[\frac{V}{2V_0} exp\left(\frac{\psi}{a}\right)\right]. \quad \text{(S3)}$$

with state variable evolution governed by:

$$\frac{d\psi}{dt} = \frac{-V}{L}\left(\psi - \psi_{ss}(V)\right), \quad \text{(S4)}$$

where the steady-state value of the state variable ψ_{ss} is given as:

$$\psi_{ss}(V) = aln\left(\frac{2V_0}{V} sinh\left(\frac{f_{ss}(V)}{a}\right)\right), \quad \text{(S5)}$$

and the steady-state value of the friction coefficient f_{ss} is given by:

$$f_{ss}(V) = f_W + \frac{f_{LV}(V) - f_W}{(1+(V/V_W)^8)^{1/8}}. \quad \text{(S6)}$$

The steady-state low-velocity friction coefficient f_{LV} depends on the reference friction coefficient f_0 and is given by:

$$f_{LV}(V) = f_0 - (b - a)ln\left(\frac{V}{V_0}\right). \quad \text{(S7)}$$

At slip rates below the characteristic weakening velocity V_w, the frictional response to slip-rate variations is governed by the standard rate-state friction parameters a and b. Materials with a-b>0 are velocity-strengthening, with frictional strength increasing in response to increased slip rate, promoting stable aseismic slip; those with a-b<0 are velocity-weakening and conditionally unstable, with frictional strength decreasing in response to increased slip rate, potentially enabling unstable seismic slip. The state variable is initialized based on the initial distributions of shear (τ_{ini}) and normal (σ_{ini}) tractions on the fault, assuming the fault is at steady-state and slipping at an initial rate V_{ini} = 10^{-16} m/s:

$$\psi_{ini} = aln\left(\frac{2V_0}{V_{ini}} \sinh \frac{\tau_{ini}}{a\sigma_{ini}}\right). \quad \text{(S8)}$$

Text S2. Mesh resolution

In numerical models of dynamic rupture, it is crucial to use a mesh with fine enough on-fault resolution to resolve the process zone or cohesive zone (e.g., Day, 1982; Wollherr et al., 2018), estimated by the distance between the propagating rupture front and the point in the slipping region behind the rupture front that has just reached its dynamic strength level. The process zone width varies spatiotemporally with different model parameters that affect

rupture velocity and total available fracture energy. Thus, for each model setup, we begin by creating a model with maximum fault element widths of 300 m, then estimate the process zone width from the results of this model. As detailed in Wollherr et al. (2018), the number of elements required to fully resolve the process zone depends on the order of the polynomial basis function used. Here, we use third-order polynomial basis functions, leading to fourth-order accuracy in space and time solving the wave equation, for which the recommended number of elements per median process zone width is 5-6. Based on these estimates, we refine the mesh until the maximum fault element size is smaller than half of the median process zone width. Final fault mesh resolutions range from ~90 m to ~150 m. The full model domain is 1,000 km x 1,000 km x 500 km, much larger than the region of interest to avoid any spurious reflected waves from the boundaries. The top boundary is a free surface and all others are absorbing. Volumetric elements away from the fault are no wider than 15 km, while those near the fault are at most 1 km wide.

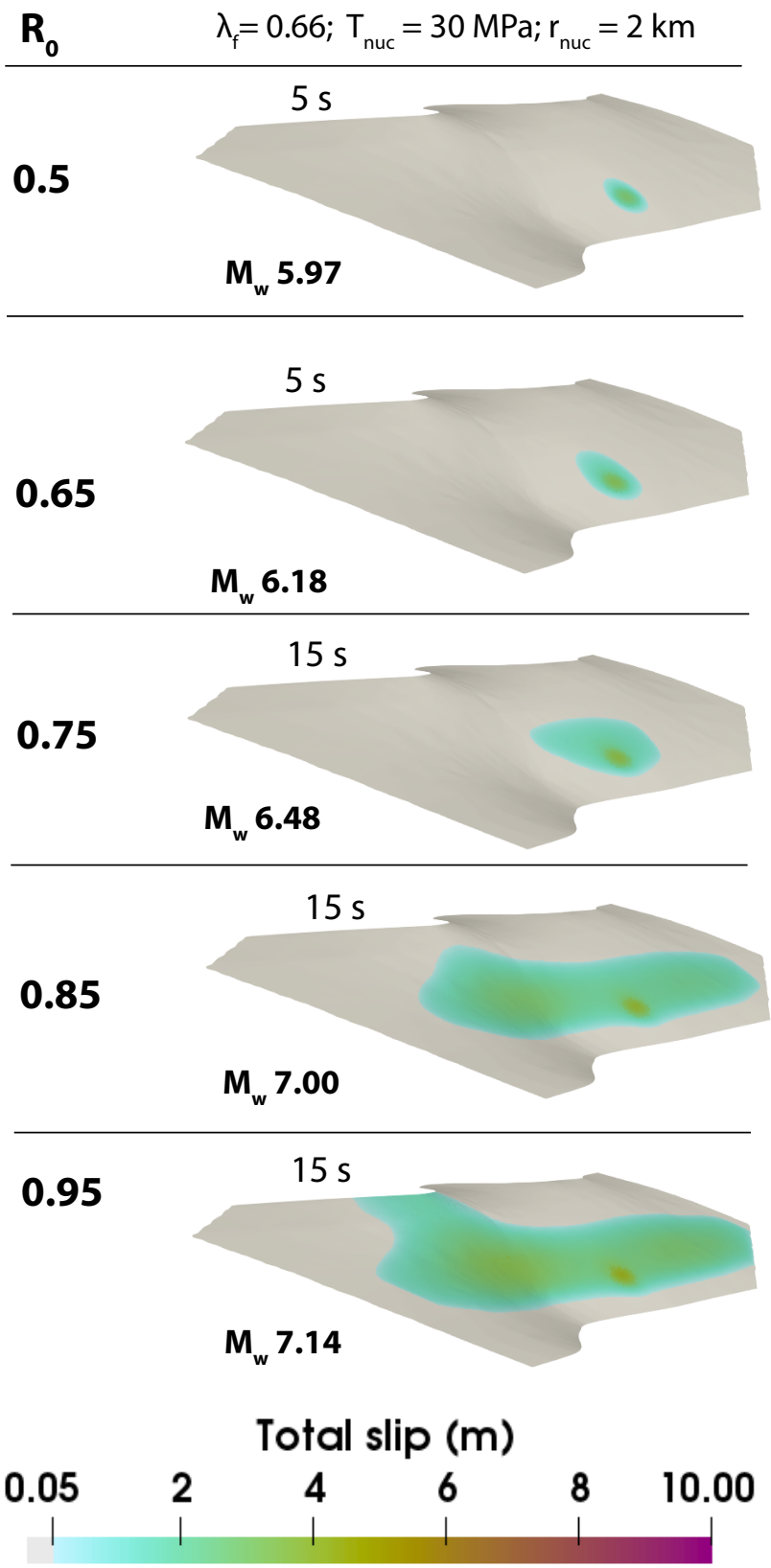

Figure S1. Model variants highlighting the rupture-limiting effect of lower closeness-to-failure as parameterized by R_0. All other model conditions are the same as in the reference model.

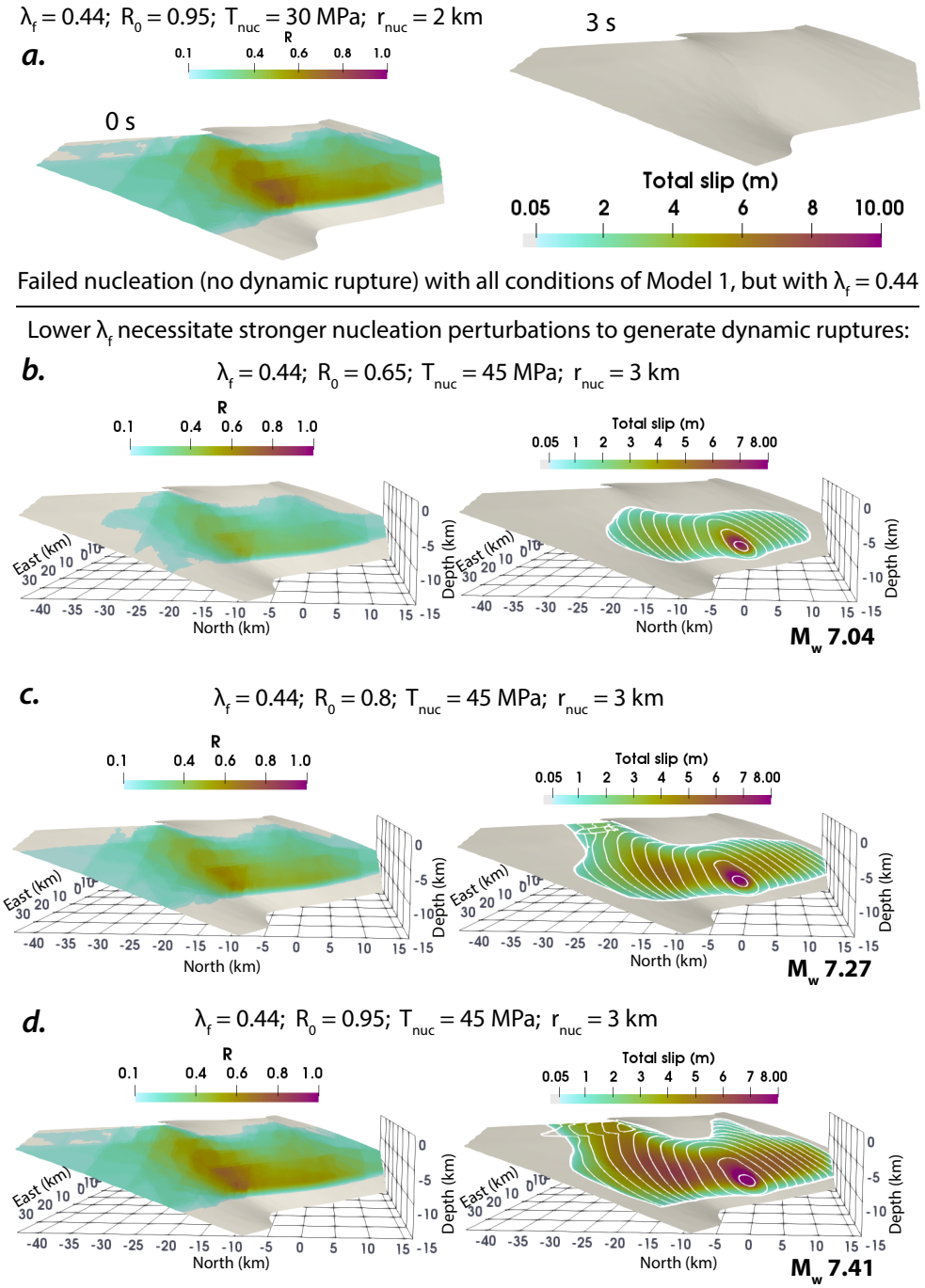

Figure S2. Prestress ratio R (left) and final slip distribution (right) with 1 s rupture contours (white) for models with lower, nearly hydrostatic pore fluid pressures of $\lambda_f = 0.44$ and a.) identical stress orientations and nucleation conditions as Model 1, which fail to nucleate dynamic rupture under such low pore fluid pressures; b-d.) nucleation tractions (45 MPa) and radii (3 km) 50% greater than those in Model 1 and initial prestress ratio $R_0 = 0.65$, 0.80, and 0.95, respectively. Slip patterns and magnitudes similar to those in model 1 emerge as R_0 increases, illustrating the tradeoffs between nucleation energy, pore fluid pressure, and initial closeness-to-failure, as well as highlighting the prevalence of these slip patterns over a wide range of initial conditions.

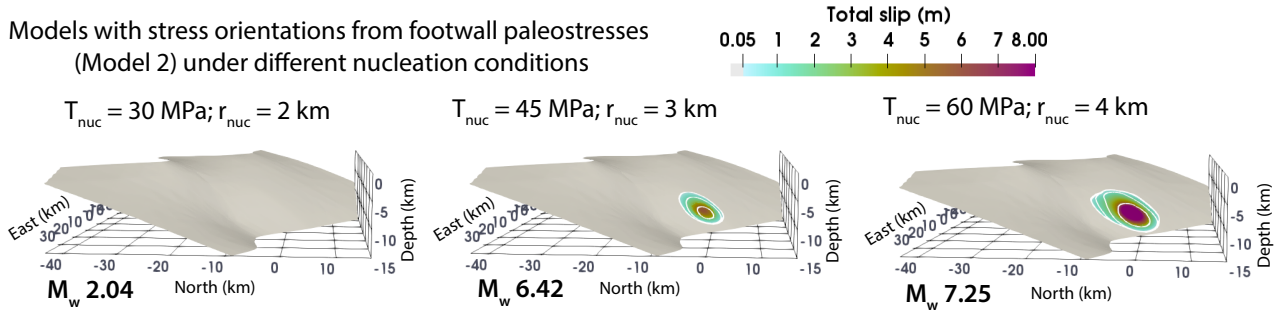

Figure S3. Models with backwards-inclined maximum principal stress (derived from Model 2) showing similarly limited slip extend under different imposed nucleation conditions. White lines show 1 s rupture contours. With nucleation conditions identical to those in the reference model, none of the fault slips more than 5 cm (left). Increasing the magnitude and area of the imposed overstress in the nucleation zone leads to greater slip in and around this zone (center, right), but does not result in ruptures that propagate away from the nucleation zone.

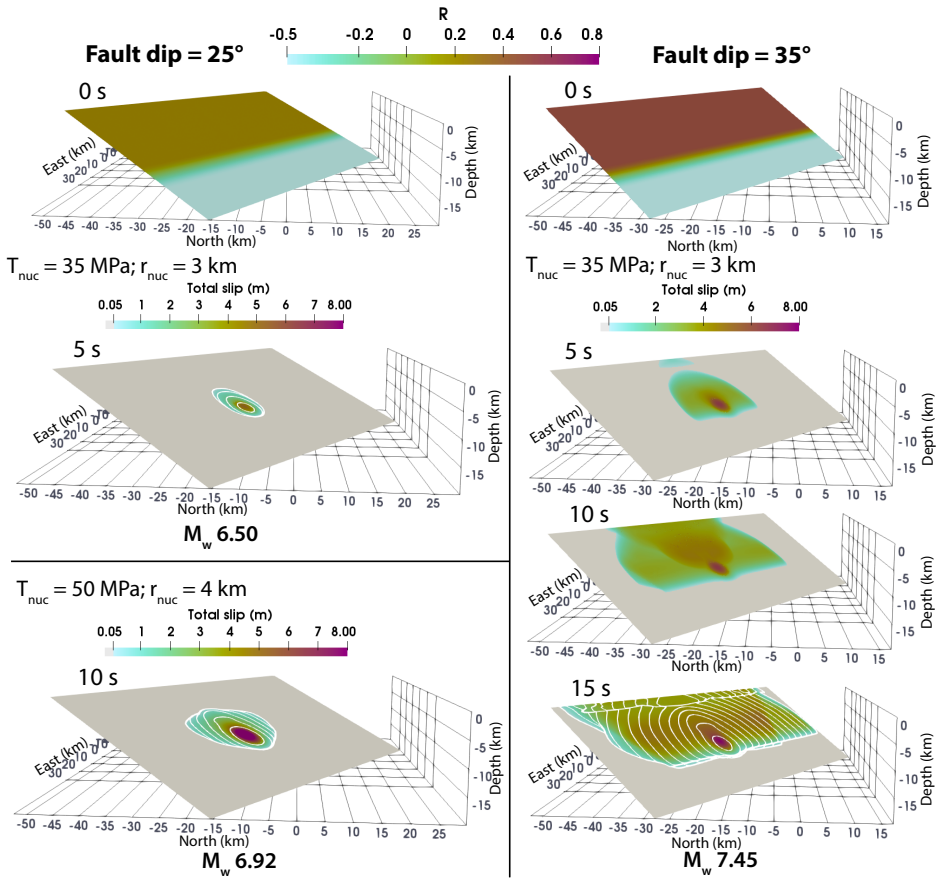

Figure S4. Models with planar detachments highlighting the effect of fault dip on slip viability. White lines show 1 s rupture contours. Identical nucleation conditions lead to full rupture of the 35°-dipping fault (right) but generate little slip outside of the nucleation zone on the 25°-dipping fault (left, center panel). Stronger nucleation conditions enable increased slip in and around the nucleation zone, but still do not lead to rupture propagation into areas much further away from this zone.

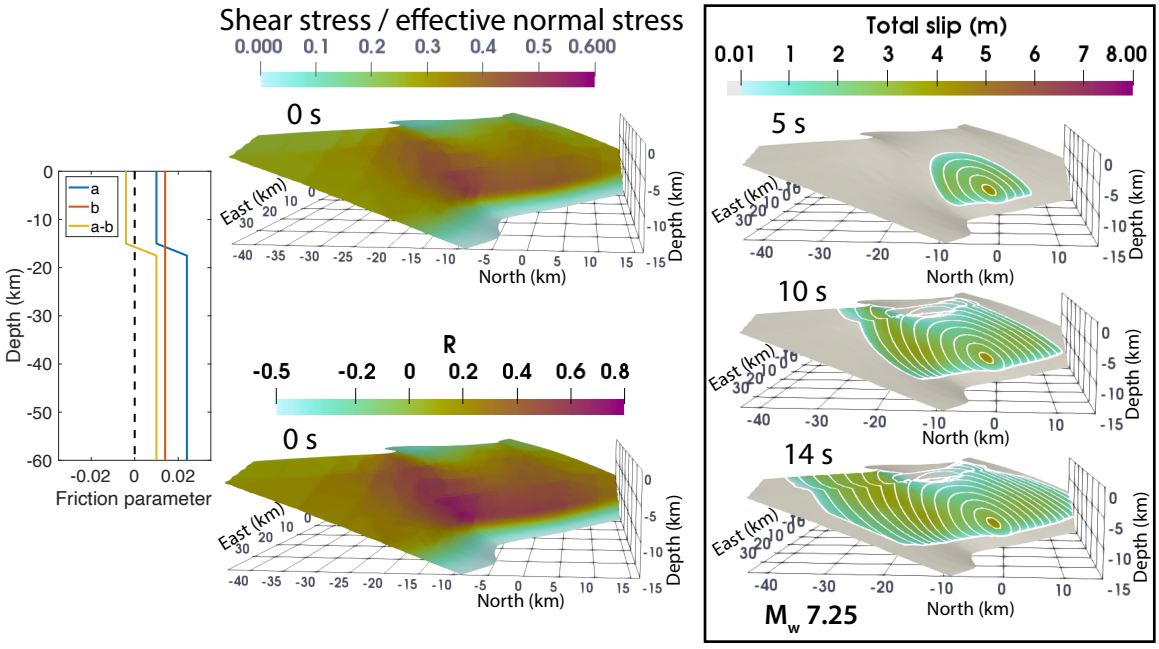

Figure S5. Model with velocity-weakening materials (a-b = -0.004, V_w = 0.1) above 15 km depth. All other model conditions are the same as those in the reference model. White lines show 1 s rupture contours. Enhanced shallow coseismic slip in this model highlights the stabilizing role of shallow velocity-strengthening gouges (Figure 2c) in limiting shallow coseismic slip in the reference model (Figure 3).

Model #	Figure #	T_{nuc}	r_{nuc}	R_0	λ_f	f_0	Stress	Plunge of σ_1	Plunge direction of σ_1	M_w	Fault geometry
		(MPa)	(km)				Andersonian extension with constant μ_s*, unless noted	(°)			Webber et al. (2020) unless noted
R1a	S1	30	2	0.5	0.66	0.6		90		5.97	
R1b	S1	30	2	0.65	0.66	0.6		90		6.18	
R1c	S1	30	2	0.75	0.66	0.6		90		6.48	
R1d	S1	30	2	0.85	0.66	0.6		90		7.00	
P1a	S2	30	2	0.95	0.44	0.6		90		1.53	
P1b	S2	45	3	0.65	0.44	0.6		90		7.04	
P1c	S2	45	3	0.8	0.44	0.6		90		7.27	
P1d	S2	45	3	0.95	0.44	0.6		90		7.41	
N2a	S3	30	2	0.95	0.66	0.6	Footwall paleostresses: backwards-inclined σ_1	15	S30°W	2.04	
N2b	S3	60	4	0.95	0.66	0.6	Footwall paleostresses: backwards-inclined σ_1	15	S30°W	7.25	
D25a	S4	30	2	0.95	0.66	0.6		90		6.50	Planar, 25° dip
D25b	S4	30	2	0.95	0.66	0.6		90		6.92	Planar, 25° dip
D35	S4	50	4	0.95	0.66	0.6		90		7.45	Planar, 35° dip
W	S5	30	2	0.95	0.66	0.6		90		7.25	

Table S1. Parameters used in the model variants shown in the Supporting Information Figures S1-S5: maximum magnitude of nucleation overstress T_{nuc}, nucleation radius r_{nuc}, initial prestress ratio R_0 (equation 1), pore fluid pressure ratio λ_f (section 2.3.3), effective static friction f_0, and resulting earthquake magnitude M_w.